ACS Catalysis

pubs.acs.org/acscatalysis Research Article

Role of the Secondary Metal in Ordered and Disordered Pt−M Intermetallic Nanoparticles: An Example of Pt_3Sn Nanocubes for the Electrocatalytic Methanol Oxidation

Hsiang-Sheng Chen, Tania M. Benedetti, Jiaxin Lian, Soshan Cheong, Peter B. O'Mara, Kazeem O. Sulaiman, Cameron H. W. Kelly, Robert W. J. Scott, J. Justin Gooding,* and Richard D. Tilley*

Cite This: *ACS Catal.* 2021, 11, 2235−2243 Read Online

ACCESS | Metrics & More | Article Recommendations | Supporting Information

ABSTRACT: When comparing alloy catalysts with different degrees of ordering, it is important to maintain surface facets to understand the effect of different arrangements of surface atoms. This is even more important when both metals are involved in the reaction steps, which is the case of Pt_3Sn for the methanol oxidation reaction (MOR). We have prepared 95 and 60% ordered Pt_3Sn nanocubes with {100} facets for the MOR. We show that the Sn atoms in the 60% ordered Pt_3Sn nanocubes can be electrochemically oxidized to Sn^{4+}, whereas the Sn atoms in the 95% ordered Pt_3Sn nanocubes are more resistant to oxidation. The Sn^{4+} in the disordered catalysts makes them more active than the ordered catalysts. At low overpotentials, the electrochemically formed Sn^{4+} in the 60% ordered Pt_3Sn nanocubes bind OH, oxidizing the CO intermediate adsorbed on Pt more efficiently. At high overpotentials, Sn^{4+} prevents the passivation of the Pt sites due to adsorption of OH. These effects lead to a 5.6 times higher activity of the 60% ordered nanocubes compared to the 95% ordered nanocubes. These results illustrate the importance in catalyst design of controlling the environment and especially the atoms neighboring Pt for intermetallic Pt−M electrocatalysts.

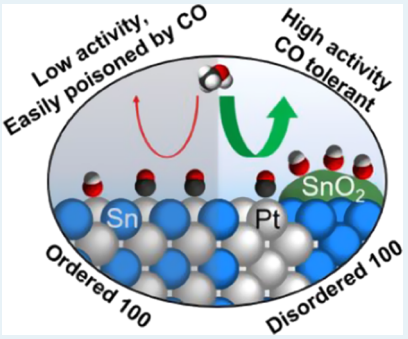

KEYWORDS: *intermetallic, Pt alloys, oxidation reaction, methanol oxidation reaction, Pt_3Sn*

INTRODUCTION

How the amount of ordering of Pt−M electrocatalysts effects activity and stability for different reactions has been a recent research focus.[1−4] Pioneering studies on Pt−Ni,[5] Pt−Co,[3] and Pt−Fe[6] systems suggesting that ordered intermetallic catalysts have higher stability and activity than their disordered counterparts.[7,8] However, there are ambiguities with these systems that limit our understanding of how different degrees of order affect catalytic performance. For these systems, a relatively high annealing temperature is usually required to achieve the disordered to ordered phase transition. This high temperature not only alters the degree of ordering but also destabilizes the surface facets.[6,9,10] As surface facets are known to have an effect on the performance for different electrocatalytic reactions,[11−13] it is best to evaluate the effect of structural order, independently of any changes to surface facets. An additional challenge is that secondary metals such as Ni, Co, and Fe dissolve into the reaction medium under the conditions used for the electrocatalysis. This can result in the formation of a pure Pt surface during the electrochemical reaction.[14−16] This dissolution hinders the performance of Pt−M catalysts in reactions where both Pt and the secondary metal are involved in critical steps of the reactions.

Herein, Sn was chosen as the secondary metal to make Pt_3Sn nanocubes. Sn was chosen because of the relatively low temperature required for the order to disorder transition and the mobility of Sn atoms. This low temperature enables alterations in the degree of ordering while maintaining other important features such as surface facets and nanoparticle size. We have previously demonstrated that it is possible to preserve the surface facets during the ordered−disordered phase transition with Pt_3Sn nanocubes. This enabled the effect of the degree of ordering on electrocatalysis to be evaluated independent of changes to surface facets.[17] It was found that under electrochemical conditions, both Pt and Sn are exposed at the surface of the nanocubes.[17] Furthermore, Sn oxide is significantly less soluble in acidic electrolyte according to its Porbaix diagram.[18] This opens up an opportunity to explore the effect of different degrees of order on reactions where both Pt and Sn are involved in a given reaction.

Received: December 7, 2020
Revised: January 23, 2021
Published: February 4, 2021

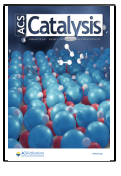

https://dx.doi.org/10.1021/acscatal.0c05370
ACS Catal. 2021, 11, 2235−2243

The methanol oxidation reaction (MOR) was chosen as the model reaction to understand the effect of ordering on reactions involving both alloy metals. For the MOR on Pt−M bimetallic systems, where M can form oxides such as RuO_xH_y or RuO_2,[19−22] SiO_2,[23] TiO_2,[24,25] CeO_2,[26−28] Mn_3O_4,[29] and SnO_2,[30] the methanol dehydrogentation step occurs on the Pt active sites to form adsorbed CO as an intermediate. Neighboring OH_{ad} from water dissociation at the metal oxide facilitates the oxidation of CO_{ad} to CO_2, resulting in higher MOR activity.

In this work, we show how the degree of ordering influences the formation of Sn oxides at the surface of Pt_3Sn nanocubes and the effect on the activity for the MOR. Our results provide a mechanistic insight into how the surface metal oxide can enhance the activity of the Pt active centers and protect Pt from being blocked by CO_{ad} and OH_{ad} during the MOR for disordered Pt_3Sn nanocubes. These results illustrate the importance of controlling the environment and the atoms neighboring Pt in the design of intermetallic Pt−M electrocatalysts.

RESULTS

Ordered Pt_3Sn nanocubes were synthesized according to our previously reported approach.[17] The low-magnification transmission electron microscopy (TEM) image in Figure S1a and the histogram in Figure S1b show that 87% of the nanoparticles are cubic in shape, which are bounded by the {100} facets. Acetic acid and thermal treatments were applied to decrease the degree of ordering while preserving the {100} facets and prevent the sintering of the nanocubes (Figure S1c−f). These TEM images, combined with the size distributions show that the cubic shape and size are maintained after the post-synthesis treatments. The X-ray diffraction (XRD) patterns of the acetic-acid-treated and the thermally treated nanocubes are shown in Figure 1a. The XRD patterns normalized by the 111 peak were used to calculate the degree of ordering from the ratio of (110) diffraction peak integration to its initial value as this peak is characteristic of the $L1_2$ ordered structure (highlighted in Figure 1b). The ratios were found to be 95% for acetic-acid-treated and 60% for thermally treated nanocubes, in agreement with our previous results.[17]

The HAADF-STEM images of a 95% ordered nanocube and a 60% ordered nanocube are shown in Figure 1c,e. The atomic arrangement of the 95% ordered nanocube in Figure 1c matches the $L1_2$ crystal structure viewing down the [100] orientation. The image of the 60% ordered nanocube in Figure 1e has areas where the atomic ordering from the $L1_2$ structure is not observable. The degree of ordering is further shown by fast Fourier transform (FFT) analysis that is shown in Figure S2a,b, respectively. In the FFTs, the 100 and 110 spots are much weaker in the 60% ordered nanocube (Figure S2b) than in the 95% ordered nanocube (Figure S2a), which again indicates the different degrees of ordering in the two samples. The location and intensity of the ordered domain (Figure 1d,f) were obtained from the inverse FFT of only the 110 spots, as indexed in Figure S2a,b. It shows that the ordered−disordered domains on the less ordered particle do not form a core−shell structure but are rather dispersed throughout the nanocube. The EDX mapping in Figure 1g,h shows the uniform distribution of Pt and Sn in the 60% ordered nanocubes.

In the Pt−Sn system, the Sn atoms are more mobile than the Pt atoms, and so the Sn atoms migrate to the surface as the structure becomes more disordered during thermal treatment.[17] As the structure becomes more disordered, the mobility of Sn increases.[31] The higher mobility of the Sn in the disordered structure results in a greater oxidized Sn-to-Pt ratio in the XPS analysis of the surface of the 60% ordered nanocubes compared to the 95% ordered nanocubes (Figure S3).

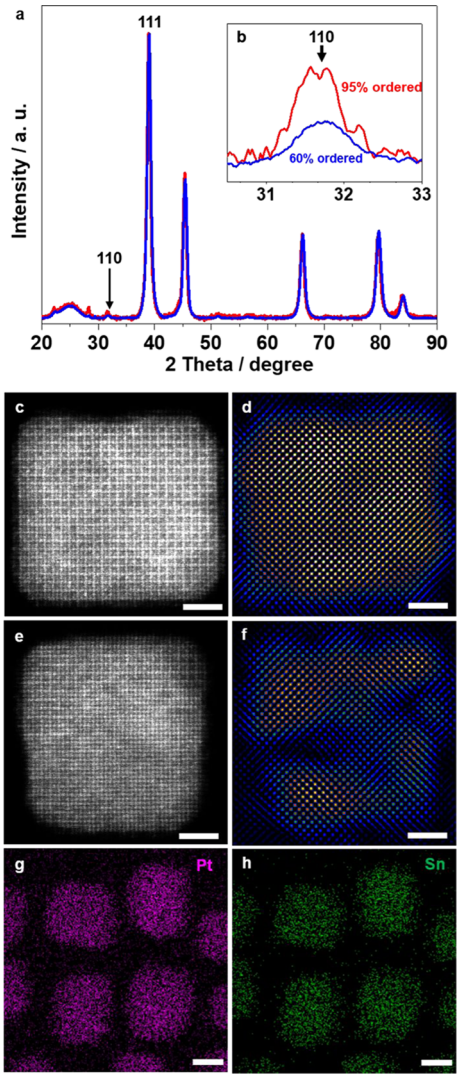

Figure 1. (a) XRD patterns of the acetic-acid-treated Pt_3Sn/C nanocubes (red) and thermally treated Pt_3Sn/C nanocubes (blue), normalized by the 111 peaks. (b) Close-up pattern of the (110) diffractions in (a), which were used to quantify the degree of ordering. (c, e) High-angle annular dark-field scanning transmission electron microscopy (HAADF-STEM) images of the 95% ordered Pt_3Sn nanocubes and the 60% ordered Pt_3Sn nanocubes; scale bar = 2 nm. (d, f) Color-graded inverse Fourier transform of Figure S2a,b by selecting only the 110 diffraction spots; scale bar = 2 nm. (g) Pt map and (h) Sn map from energy-dispersive X-ray spectroscopy (EDX) mapping of the 60% ordered Pt_3Sn nanocubes on C; scale bar = 5 nm.

Before performing the electrocatalytic measurements, the Pt_3Sn nanocubes were activated by cyclic voltammetry in two different electrolytes, 0.1 mol L^{-1} $HClO_4$ and 0.1 mol L^{-1} KOH, to give different amounts of Sn oxide at the surface of the nanocubes. Under acidic conditions, oxidation of Sn results in the formation of insoluble SnO_2, whereas under alkaline conditions, oxidation of Sn results in its dissolution into the electrolyte.[32]

https://dx.doi.org/10.1021/acscatal.0c05370
ACS Catal. 2021, 11, 2235−2243

No observable changes in the size and morphology of either 60 or 95% ordered nanocubes were observed after the activation processes, as shown by the identical-location HAADF-STEM image and low-magnification TEM image in Figure S4. Also, no differences in strain were observed based on the same bond length of the Pt−Pt between the 60% ordered nanocubes and the 95% nanocubes using edge X-ray absorption fine structure (EXAFS) and pair distribution function (Table S1).

The resulting ratios of Sn^{4+} to Pt after the different activation processes on both nanocubes were obtained from the integration of the fitted peaks in the Sn $3d_{5/2}$ region of the XPS spectra presented in Figure 2a for the 60% ordered

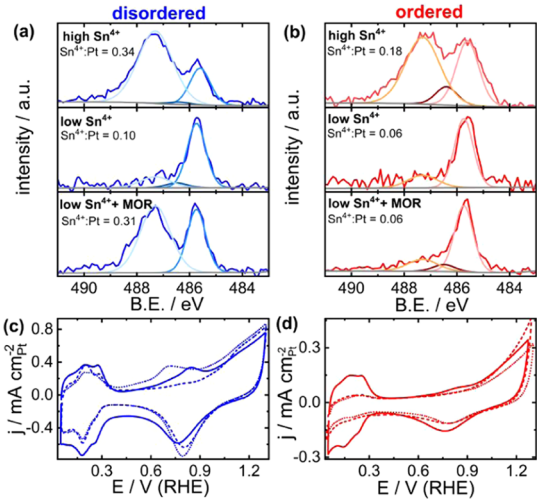

Figure 2. Fitted Sn $3d_{5/2}$ XPS spectra of (a) the 60% ordered and (b) 95% ordered Pt_3Sn nanocubes after activation in 0.1 mol L^{-1} $HClO_4$ (high Sn^{4+}), after activation in 0.1 mol L^{-1} KOH (low Sn^{4+}) and after activation in 0.1 mol L^{-1} KOH + 10 voltammetric cycles between 0.05 and 1.3 V (RHE) in 0.1 mol L^{-1} $HClO_4$ and 1.0 mol L^{-1} methanol (low Sn^{4+} + MOR). The spectra were fitted to give the contribution of Sn^0 (485.6 eV), Sn^{2+} (486.4 eV), and Sn^{4+} (487.3 eV). Cyclic voltammograms of (c) the 60% ordered Pt_3Sn nanocubes and (d) the 95% ordered Pt_3Sn nanocubes. The full line is after activation in $HClO_4$ (high Sn^{4+}), the dashed line after activation in KOH (low Sn^{4+}), and the dotted line after activation in KOH + 10 cycles in $HClO_4$ + methanol (low Sn^{4+} + MOR); electrolyte: 0.1 mol L^{-1} $HClO_4$; scan rate = 50 mV s^{-1}.

nanocubes and in Figure 2b for the 95% ordered nanocubes. The results show that a higher ratio of Sn^{4+} to Pt is obtained after activation in the acidic electrolyte than in the alkaline electrolyte, giving nanocubes with four different surfaces: the 60% ordered nanocubes with Sn^{4+}-to-Pt ratios of 0.34 and 0.10, and the 95% ordered nanocubes with Sn^{4+}-to-Pt ratios of 0.18 and 0.06. We will call these nanocubes "disordered high Sn^{4+}", "disordered low Sn^{4+}", "ordered high Sn^{4+}", and "ordered low Sn^{4+}", respectively.

The ratio of Sn^{4+} to Pt of 0.34 (Figure 2a) for the disordered high Sn^{4+} nanocubes is similar to the as-prepared particles (Figure S3). Also, inductively coupled plasma mass spectrometry (ICP-MS) analysis of the electrolyte after the activation in KOH to produce the ordered and disordered low Sn^{4+} nanocubes shows that less than 0.2% of Pt was dissolved on both samples (Figure S5), which means that the decrease of the ratio of Sn^{4+} to Pt is predominantly due to the dissolution of Sn^{4+}.

The cyclic voltammograms in acidic electrolyte of both disordered high Sn^{4+} (Figure 2c, full line) and ordered high Sn^{4+} (Figure 2d, full line) nanocubes present an oxidation peak at 0.84 V. Although the oxidation peak is at the same potential for both ordered high Sn^{4+} and disordered high Sn^{4+} nanocubes, the peak current density is significantly lower for the ordered nanocubes. Also, the oxidation peak at 0.84 V is absent in the disordered low Sn^{4+} (dashed line in Figure 2c) and ordered low Sn^{4+} nanocubes (dashed line in Figure 2d). This oxidation peak has been previously observed for other alloys such as Pt−Ni, Pt−Co, and Pt−Cr, and has been correlated with the degree of ordering, with higher currents indicating more disordered structures.[5,33−35] However, our results show a correlation between the oxidation peak and the presence of Sn^{4+} at the surface that is independent of the degree of ordering, suggesting that the peak possibly corresponds to OH adsorption at the SnO_2 sites. This suggestion that the peak corresponds to adsorption of OH groups derived from water at the surface of the catalyst is supported by Chung et al.[10]

The ratio of Sn^{4+} to Pt of the disordered low Sn^{4+} nanocubes increases from 0.10 to 0.31 after 10 MOR cycles in acid electrolyte, as shown in Figure 2a, becoming similar to the Sn^{4+}-to-Pt ratio in the disordered high Sn^{4+} nanocubes. This is accompanied by the appearance of an oxidation peak at 0.71 V after the 10 MOR cycles. (Figure 2c dotted line). In contrast, the Sn^{4+}-to-Pt ratio is maintained for the ordered low Sn^{4+} nanocubes after the 10 MOR cycles (Figure 2b) and no peak ascribed to OH adsorption can be found in the cyclic voltammogram, as shown in Figure 2d (dotted line). This suggests that the Sn atoms in the disordered domain are more easily oxidized than in the ordered domains under the MOR conditions used here. The results show that the Sn atoms in the ordered domain are highly resistant to electrochemical oxidation.

The effect of the amount of surface Sn^{4+} on MOR activity was evaluated by cyclic voltammetry of the Pt_3Sn nanocubes in 0.1 mol L^{-1} $HClO_4$ electrolyte containing 1 mol L^{-1} methanol. The obtained voltammograms presented in Figure 3 show the typical two MOR oxidation peaks, one in the anodic direction and the other in the cathodic direction for all samples.[36] In general, the specific current densities are higher for the samples with a higher Sn^{4+} amount, suggesting that the presence of Sn^{4+} at the surface of the catalysts positively influences the

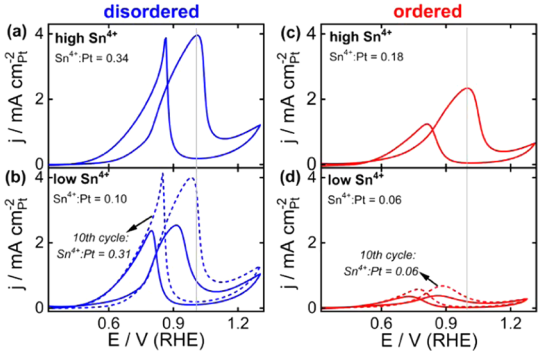

Figure 3. Cyclic voltammograms in 0.1 mol L^{-1} $HClO_4$ + 1 mol L^{-1} methanol of (a) disordered high Sn^{4+}, (b) disordered low Sn^{4+}, (c) ordered high Sn^{4+}, and (d) ordered low Sn^{4+} nanocubes. Scan rate = 50 mV s^{-1}; full lines = first cycle, dashed lines = 10th cycle. The Sn^{4+}:Pt ratios were obtained by integration of XPS Sn $3d_{5/2}$ peaks.

https://dx.doi.org/10.1021/acscatal.0c05370
ACS Catal. 2021, 11, 2235−2243

Scheme 1. Schematic Illustration of the Relevant Species Involved in Methanol Oxidation Reaction at Different Potentials along the Anodic Voltammetry Scan on the Disordered (Top—Blue) and Ordered (Bottom—Red) Pt_3Sn nanocubes[a]

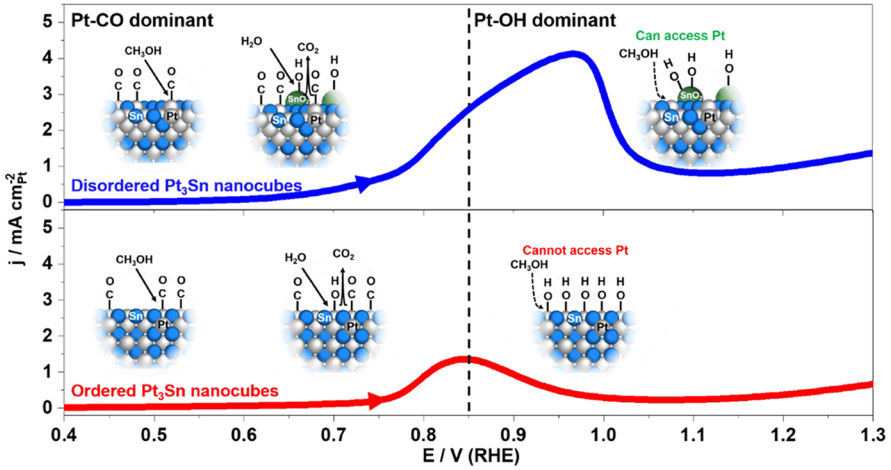

[a]The dotted line marks the potential of 0.85 V, roughly separating the potential range where Pt−CO* (less positive than 0.85 V) or Pt−OH* (more positive than 0.85 V) dominates at the surface for pure Pt.

MOR activity. By comparing between the samples with the same degree of ordering but different Sn^{4+} amounts, the specific activities (charge obtained from integration of the peak current in the anodic direction divided by the electrochemical surface area (ECSA) of Pt) are initially higher for the nanocubes with high Sn^{4+} than for the ones with low Sn^{4+}. With the disordered nanocubes, these are 23.0 and 10.2 mC cm^{-2} for the ones with high Sn^{4+} and low Sn^{4+}, respectively. The specific activity of the disordered nanocubes with high Sn^{4+} is comparable to the recently reported Pt-based nanocatalysts.[37−39]

With the ordered nanocubes, the values are 10.0 and 4.3 mC cm^{-2} for the cubes with high Sn^{4+} and low Sn^{4+}, respectively. In addition to the differences in specific activities, for both nanocubes with high Sn^{4+}, the anodic peak is positioned at 1.00 V (marked with vertical gray lines in Figure 3), which is 90 and 140 mV more positive than the oxidation peak in the first voltammetric cycle of the disordered low Sn^{4+} (full line in Figure 3b) and ordered low Sn^{4+} (full line in Figure 3d) nanocubes, respectively.

The specific current densities increase in the subsequent cycles for both disordered low Sn^{4+} and ordered low Sn^{4+} nanocubes, becoming stable after around 10 cycles (dashed lines in Figure 3b,d for the disordered and ordered nanocubes, respectively). For the disordered low Sn^{4+} nanocubes, the specific activity increases to 28 mC cm^{-2} after 10 cycles, becoming slightly higher than the specific activity of the disordered high Sn^{4+} nanocubes (23 mC cm^{-2}). This increase in specific activity after 10 cycles is accompanied by a shift of the anodic peak potential from 0.91 to 0.98 V, becoming closer to the peak at 1.00 V observed for the disordered high Sn^{4+} nanocubes (Figure 3a). The Sn^{4+}-to-Pt ratio after 10 MOR cycles increases to 0.31, which is similar to the ratio of the disordered high Sn^{4+} nanocubes (Figure 2a). Note that the current densities were normalized by the Pt ECSA after each cycle, so the changes in activity are not related to changes in the amount of Pt at the surface but the actual intrinsic activity of the sites at the surface.

In comparison to the disordered low Sn^{4+}, the ordered low Sn^{4+} nanocubes show a lesser increase in activity after 10 MOR cycles, increasing to only 5.8 mC cm^{-2} after 10 cycles (compared with 10 mC cm^{-2} for the ordered high Sn^{4+} nanocubes). The anodic oxidation peak potential also only exhibited a small shift from 0.86 to 0.89 V, which is significantly less positive than the 1.00 V peak potential of the ordered high Sn^{4+} nanocubes (Figure 3c). Also, no increase in the Sn^{4+}:Pt ratio (Figure 2b) was observed.

Pure Pt nanocubes of a similar size to the ordered and disordered Pt_3Sn nanocubes discussed thus far (10.4 ± 0.5 nm) and bounded by the identical {100} exposed facets (Figure S6) activated in either acidic or alkaline electrolyte show similar specific activity to the ordered nanocubes with low Sn^{4+} (Figures S7 and S8). The similar activities between the Pt nanocubes and the ordered low Sn^{4+} nanocubes suggest that possible influences of strain or electronic effect from alloying Sn with the Pt active sites are negligible and that Sn^{4+} present at the surface plays a more significant role in the improved MOR performance.

DISCUSSION

The higher specific activity provided by the presence of Sn^{4+} at the surface of the catalysts is accompanied by a positive shift of the oxidation peak in the anodic direction. A closer look into the peak at 0.98 V of the disordered low Sn^{4+} after 10 MOR cycles (Scheme 1, blue line—top) shows that it presents a shoulder around 0.85 V, which is a similar potential to the oxidation peak at the ordered low Sn^{4+} after 10 MOR cycles (Scheme 1, red line—bottom). This suggests that the greater current with increasing Sn^{4+} is actually accompanied by the appearance of a second oxidation process that arises due to a different mechanistic pathway. We hypothesize the peak asymmetry is due to a second pathway facilitated by the presence of Sn^{4+} at potentials more positive than 0.85 V. SnO_2 alone is incapable of oxidizing either methanol or CO at potentials more positive than 0.85 V, as shown by the CO stripping and MOR measurements using SnO_2 nanoparticles (Figure S9). Thus, the greater current density at potentials more positive than 0.85 V is related to how the surface Sn^{4+} assists in keeping the Pt sites active at higher overpotentials.

At potentials less positive than 0.85 V (Scheme 1, left), water dissociation to produce OH_{ad} (eq 2) is the rate-determining step for the MOR.[36] With the disordered high

https://dx.doi.org/10.1021/acscatal.0c05370
ACS Catal. 2021, 11, 2235−2243

Sn^{4+} nanocubes, water dissociation happens mostly at the SnO_2 sites instead of the Pt sites and the CO_{ad} oxidation to CO_2 (eq 3) on Pt is facilitated by the presence of OH_{ad} at the surface of SnO_2. This leads to a lower onset potential with a 60 mV lower overpotential required to reach 0.15 mA cm^{-2} than that required for the ordered nanocubes (0.64 and 0.70 V for the disordered low Sn^{4+} and ordered low Sn^{4+}, respectively, both after 10 MOR cycles). The CO stripping by linear sweep voltammetry in Figure S10a and the percentage of CO oxidized at different potentials in Figure S10b also show that the disordered nanocubes can oxidize more CO_{ad} at less positive potentials than the ordered nanocubes, which agree with previously reported cases where higher coverage of Sn on Pt electrodes enhances CO oxidation at lower overpotentials.[40,41]

$$CH_3OH + Pt \rightarrow Pt - CO_{ad} + 4H^+ + 4e^- \quad (1)$$

$$H_2O + M \rightarrow M - OH_{ad} + H^+ + e^- \quad (2)$$

$$Pt - CO + M - OH \rightarrow Pt^* + M^* + CO_2 + H^+ + e^- \quad (3)$$

At potentials more positive than 0.85 V (Scheme 1, right), methanol adsorption and oxidation at the Pt sites (eq 1) becomes the rate-determining step as the formation of Pt−OH_{ad} becomes significant, blocking methanol from accessing the Pt active sites.[36] In the disordered nanocubes, the high coverage of OH_{ad} on the Sn^{4+} seems to prevent the Pt active sites from being blocked by OH_{ad}, allowing the MOR to proceed via the no longer limited methanol dehydrogenation (eq 1) at potentials more positive than 0.85 V (Scheme 1, top right),[42−44] as opposed to the ordered low Sn^{4+} nanocubes, where the high Pt−OH_{ad} causes the MOR rate to decrease from potentials more positive than 0.85 V (Scheme 1, bottom right).

CO tolerance is an important factor in assessing the industrial value of the catalysts for the direct methanol fuel cells (DMFCs). Since CO is a common intermediate in methanol production, this is often present in the fuel[45−47] and concentrations of CO as low as 10 ppm in the electrolyte are sufficient to deactivate Pt-based catalysts at the anode of DMFCs.[45] The anodic scan of the voltammograms of the Pt_3Sn nanocubes presented in Figure 4 shows how the current densities are affected when the MOR is performed in Ar- (dashed lines) and CO- (full lines) saturated electrolytes. It can be observed in Figure 4a that with the disordered nanocubes, the peak position does not change with 60% of its current density at 0.8 V maintained after CO saturation. In contrast, for the ordered Pt_3Sn and Pt nanocubes, the peak has shifted to more positive potentials from 0.85 to 1.01 V (Figure 4b) and 0.87 to 1.00 V (Figure 4c), respectively, and the MOR is heavily suppressed between 0.6 and 1.0 V. The fact that the reaction is suppressed at potentials less positive than 1.00 V in CO-saturated electrolyte suggests that the MOR cannot proceed via CO_{ad} oxidation to CO_2 (eq 3) at the ordered Pt_3Sn and Pt nanocubes. Under Ar-saturated electrolyte, although the Pt sites are partially covered with CO_{ad}, the MOR is still possible via the alternative formate pathway as these two pathways occur in parallel.[48] In fact, the ordered Pt_3Sn nanocubes and Pt nanocubes have more than 3 times higher faradic efficiency in producing formic acid at 0.7 V in Ar-saturated electrolyte than the disordered Pt_3Sn nanocubes (Figure S11), showing the more important contribution of formate formation compared to CO_{ad} oxidation to the total MOR charge.

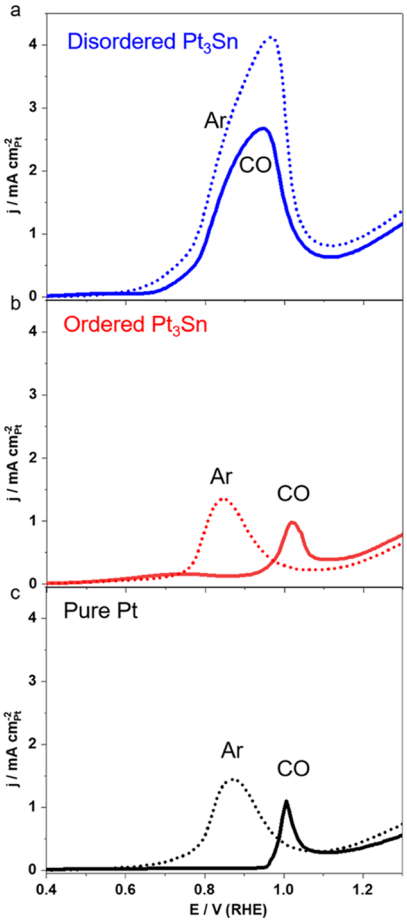

Figure 4. Anodic scans of cyclic voltammograms in 0.1 mol L^{-1} $HClO_4$ + 1 mol L^{-1} methanol electrolyte saturated with Ar (dotted curves) or CO (solid curves); disordered Pt_3Sn nanocubes (a), ordered Pt_3Sn nanocubes (b), and Pt nanocubes (c). Scan rate = 50 mV s^{-1}.

By maintaining the size and exposed facets of Pt_3Sn nanocubes during disordered to ordered transition, we were able to study the effect of degree of ordering on the formation of surface SnO_2 and its relationship with MOR activity, where both Pt and secondary metal participate in the reaction. It was shown that the Sn atoms at the disordered sites are more easily oxidized to form more surface Sn^{4+} than the Sn at the ordered sites. The formation of the surface Sn^{4+} not only facilitates the oxidation of CO_{ad} to CO_2 but also prevents the deactivation of the Pt sites caused by OH_{ad}. These results show that ordered catalysts are not necessarily more active than their disordered counterpart and that tuning the degree of ordering, especially when both metals are functional in a reaction, is vital to achieve better performance using alloy catalysts. These results illustrate the importance of controlling the neighboring atoms surrounding active species such as Pt, especially when those neighbors play a role in the reaction. Designing catalysts with control of neighboring atoms is an important concept that can guide design of future catalysts all the way from single-atom catalysts on specific supports to bimetallic nanoparticles.

https://dx.doi.org/10.1021/acscatal.0c05370
ACS Catal. 2021, 11, 2235−2243

EXPERIMENTAL SECTION

Synthesis of Pt_3Sn Nanocubes and Formation of the 60% and 95% Ordered Pt_3Sn Nanocubes/C Catalysts. A modified hot injection approach was used to synthesize the ordered Pt_3Sn nanocubes.[49] First, tetradecanediol (66.8 mg, 90%, Sigma-Aldrich) and dodecylamine (300 mg, 98%, Sigma-Aldrich) were mixed with 1-octadecene (3 mL, 90%, Sigma-Aldrich) in a 25 mL two-neck flask. The solution was then heated to 240 °C in an argon environment (Air Liquide) under mild stirring. Meanwhile, $PtCl_2$ (11.5 mg, 98%, Sigma-Aldrich) and $SnCl_2{\cdot}2H_2O$ (10 mg, 98%, Sigma-Aldrich) were each mixed with 2.5 mL of 1-octadecene and 100 mg of dodecylamine using sonication and gentle mixing. Then, 2.25 mL of $PtCl_2$ solution was mixed with 0.75 mL of $SnCl_2{\cdot}2H_2O$ solution and sonicated for 30 s; then, 2 mL of the mixed solution was injected into the two-neck flask at 0.2 mL min^{-1}. The reaction was maintained at 240 °C for 10 min after the injection finished. Finally, the flask was cooled to room temperature and the particles were washed two times with a 1:1 mixture of isopropanol and *n*-hexane.

The synthesized particles were then supported on carbon Vulcan (XC72, Fuel cell Store) by sonication for 2 h followed by overnight vigorous mixing of the synthesized particles dispersed in *n*-hexane and oleylamine with the carbon powder. Then, the catalyst was washed twice with a 1:1 mixture of *n*-hexane and isopropanol. The final catalyst consists of 15−20 wt % Pt, as determined by ICP-MS.

The oleylamine was removed from the fully ordered Pt_3Sn NCs/C catalyst by stirring it in 10 mL of acetic acid at 70 °C for 10 h, which resulted in a degree of ordering of 95%. The acetic-acid-treated catalyst was then washed twice with a 1:1 mixture of *n*-hexane and isopropanol and dried by a rotary evaporator. To obtain the Pt_3Sn NCs/C catalyst with 60% degree of ordering, the fully ordered Pt_3Sn NCs/C catalyst was thermally treated in a tube furnace at 200 °C for 5 h under airflow, which also removed the oleylamine from the nanoparticles surface.[50]

Synthesis of Pt Nanocubes/C Catalyst. Pt nanocubes were synthesized by modifying a reported procedure.[51] Platinum(II) acetylacetonate (9.8 mg, 98%, Sigma-Aldrich) was dispersed in a solution of oleylamine (4 mL, 70%, Sigma-Aldrich) and oleic acid (1 mL, 90%, Sigma-Aldrich) in a 25 mL two-neck flask connected with a condenser. The mixture was then stirred gently and heated to 130 °C within 30 min under an Ar environment. $W(CO)_6$ (25 mg, 97%, Sigma-Aldrich) was added into the solution after the temperature reached 130 °C. The solution was then heated to 240 °C within 15 min and kept at 240 °C for 40 min. Finally, the reaction was cooled down to room temperature and the particles were washed three times with a 1:1 mixture of isopropanol and *n*-hexane. Then, the particles were supported on carbon and thermally treated at 200 °C to remove the surfactant using the same procedure for the Pt_3Sn nanocubes.

Synthesis of SnO_2/C Catalyst. SnO_2 nanoparticles were prepared by modifying a reported hydrothermal synthesis.[52] $SnCl_4{\cdot}5H_2O$ (82 mg, 99%, Sigma-Aldrich) was mixed with 8 mL of isopropanol and KOH aqueous solution (2 mL, 0.05 mol L^{-1}, Sigma-Aldrich). The mixture was then placed in a high-pressure glass tube sealed with a Teflon cap and heated in an oil bath to 125 °C, which was slowly increased to 150 °C in 10 min and kept at 150 °C for 24 h. The particles were washed twice with ethanol, and 2 mg of SnO_2 nanoparticles was then mixed with 8 mg of carbon Vulcan and 10 mL of ethanol, sonicated for 2 h, and stirred vigorously overnight. Finally, the SnO_2/C catalyst was washed twice with ethanol and dried using a rotary evaporator.

Characterizations of Synthesized Nanoparticles. The XRD patterns were acquired using an MPD (PANalytical) X'Pert multipurpose X-ray diffraction system with Cu Kα X-rays. X-ray photoelectron spectroscopy (XPS) characterization was performed on an ESCALab 250 Xi (Thermo Scientific) spectrometer with a monochromatic Al Kα source. The pressure in the analysis chamber during measurement was $<10^{-8}$ mbar. The pass energy and step size for narrow scans were 20 and 0.1 eV, respectively, with a takeoff angle normal to the sample surface. Spectral analysis was performed using Avantage 4.73 software and curve fitting was carried out with a mixture of Gaussian−Lorentzian functions. The peaks were calibrated to C−C at 284.5 eV. TEM images were obtained using an FEI Tecnai G2 20 (200 kV, thermionic LaB6 source), and STEM images and EDX mapping were obtained with a JEOL JEM-F200 (200 kV, cold field emission gun) equipped with an annular dark-field (ADF) detector and a windowless silicon drift X-ray detector. STEM images were acquired with a convergence semiangle of 8.2 mrad, and an ADF inner collection angle of 62 mrad (for achieving high-angle Z-contrast conditions). EDX data were analyzed and processed using the Pathfinder X-ray microanalysis software (Thermo Scientific). X-ray absorption spectroscopy (XAS) measurements were conducted on the Biological X-ray absorption spectroscopy (BioXAS) beamline (energy range: 4−32 keV; resolution: 1×10^{-4} $\Delta E/E$; spot size: 5 mm × 0.5 mm) at the Canadian Light Source. Samples were loaded into sample holders under Ar to prevent air exposure prior to measurements. Energy selection was done using a Si (220) double-crystal Si monochromator, with a water-cooled toroidal Rh-coated Si mirror before the monochromator and a second Rh-coated Si (focusing) mirror after the monochromator. Ionization chambers were filled with Ar, and samples were measured in fluorescence using a 32-element Ge detector. X-ray energies were calibrated using Sn and Pt foils for their K- and L3-edge measurements, respectively. The data processing was performed using the IFEFFIT software package.[53] The amplitude reduction factor was found to be 0.80 and 0.86 for Sn and Pt, respectively.

Setup for Electrochemical Measurements. All experiments were performed using a μAutolab potentiostat controlled with Nova 2.1.2 software with a three-electrode assembly consisting of a Pt mesh as the counter electrode and a Ag|AgCl|3 mol L^{-1} NaCl as the reference electrode for acidic electrolyte, or a Hg|HgO|1 mol L^{-1} NaOH as the reference electrode for alkaline electrolyte. $HClO_4$ (0.1 mol L^{-1}, Suprapur, Merck) was used as the acidic electrolyte, and KOH (0.1 mol L^{-1}, reagent grade, Sigma-Aldrich) was used as the alkaline electrolyte. The cell was saturated with Ar or CO during the experiments. All potentials are referred against the reversible hydrogen electrode (RHE) and were converted by measuring the potential difference between the reference electrode and a freshly prepared normal hydrogen electrode (NHE).

For ink preparation, 1 mg of carbon-supported catalyst was mixed with 20 μL of Nafion 0.5 wt % in isopropanol solution, 80 μL of isopropanol, and 300 μL of deionized water. The resulting ink (6 μL) was then drop-cast uniformly on the glassy carbon surface (0.07 cm^2) as the working electrode.

https://dx.doi.org/10.1021/acscatal.0c05370
ACS Catal. 2021, 11, 2235−2243

The electrochemically active surface area (ECSA) was obtained by CO stripping by applying 0.05 V (RHE) for 15 min in a CO-saturated 0.1 mol L^{-1} $HClO_4$, followed by three cycles of cyclic voltammetry between 0.05 and 1.3 V (RHE) in Ar-saturated 0.1 mol L^{-1} $HClO_4$ to confirm that all CO_{ad} were oxidized in the first cycle. The baselines were obtained by performing the exact procedure but in the absence of CO. Then, the current of CO oxidation was subtracted from the baseline and integrated to obtain the charge that was converted into ECSA using 420 μC cm^{-2} as correlation.[54]

Electrochemical Removal of SnO_x-Rich Surface of Pt_3Sn/C Catalysts. To remove the SnO_x-rich surface formed during thermal and acetic acid treatments, five cycles of cyclic voltammetry in 0.1 mol L^{-1} KOH between 0.1 and 1.3 V (RHE) at 50 mV s^{-1} were performed,[32] after which no notable differences in the voltammograms profiles were observed after the third cycle, indicating that the SnO_x-rich surface has been removed.

Identical-Location HAADF-STEM Imaging. HAADF-STEM imaging of the same particle before and after KOH electrochemical treatment was carried out with unsupported nanoparticles. The particles were deposited on a Au TEM grid; then, the grid was fixed on a glassy carbon surface using carbon tape that was subsequently covered with acrylated varnish. The heart-shaped mark at the center of the TEM grid and uniquely shaped clusters were used for navigation, tracking the same particle before and after the KOH treatment. The magnification was kept below 120 k X except when taking high-magnification images to reduce beam damage and contamination. A frame size of 512 × 512 pixels and a dwell time of 30 μs were used to strike a balance between resolution and sample drifting for high-magnification imaging.[17]

Methanol Oxidation Reactions Electrocatalysis. The methanol oxidation measurements were performed after the KOH treatment, except for the non-KOH-treated plots, which was activated by 20 cycles of potential scans between 0.05 and 1.3 V in 0.1 mol L^{-1} $HClO_4$. In a typical experiment, 10 cycles of cyclic voltammetry were performed in Ar- or CO-saturated 0.1 mol L^{-1} $HClO_4$ + 1 mol L^{-1} methanol between 0.05 and 1.3 V (RHE) at 50 mV s^{-1}; then, CO stripping was performed to estimate the ECSA.

Postelectrocatalysis Characterizations. For the XPS analysis, 2 mL of catalyst ink was deposited on the lower half of a 5 cm × 5 cm glassy carbon surface. The surface was then wetted with a 9:1 water:ethanol solution, and the uncoated half of the glassy carbon was used to connect to the potentiostat using an alligator clip. After KOH treatment, the glassy carbon was sonicated in isopropanol to retrieve the catalysts, centrifuged at 7000 rpm, washed three times with ethanol to remove the electrolyte, dried, and kept in a vacuum desiccator. The electrolyte used for KOH treatment was analyzed by ICP-MS using a Nexion ICP-MS PerkinElmer instrument to calculate the amount of dissolved Sn and Pt species. The same process was applied for XPS analysis after the methanol oxidation reaction measurements.

Quantifying the Formic Acid Formed in Electrolyte Using NMR. Liquid products were analyzed using 1H-NMR; 540 μL aliquots of electrolyte were taken after electrocatalysis. Each aliquot was mixed with 60 μL of dimethyl sulfoxide (DMSO) in D_2O stock solution. The DMSO in D_2O stock solution was prepared by mixing 5.0 μL of DMSO with 10 mL of D_2O. NMR aliquots were investigated on a Bruker Avance III 400 MHz NMR spectrometer with 64 scans and a 16 s recycle delay, using DMSO as the internal standard. Product quantification was performed via the internal DMSO standard to determine the concentration of formic acid.

■ ASSOCIATED CONTENT

Supporting Information

The Supporting Information is available free of charge at https://pubs.acs.org/doi/10.1021/acscatal.0c05370.

Experimental details, additional characterizations, and calculations (PDF)

■ AUTHOR INFORMATION

Corresponding Authors

J. Justin Gooding − *School of Chemistry and Australian Centre for NanoMedicine and Australian Research Council Centre of Excellence in Convergent Bio-Nano Science and Technology, University of New South Wales, Sydney 2052, Australia;* orcid.org/0000-0002-5398-0597; Email: justin.gooding@unsw.edu.au

Richard D. Tilley − *School of Chemistry and Australian Centre for NanoMedicine and Mark Wainwright Analytical Centre, University of New South Wales, Sydney 2052, Australia;* orcid.org/0000-0003-2097-063X; Email: r.tilley@unsw.edu.au

Authors

Hsiang-Sheng Chen − *School of Chemistry and Australian Centre for NanoMedicine, University of New South Wales, Sydney 2052, Australia*

Tania M. Benedetti − *School of Chemistry and Australian Centre for NanoMedicine, University of New South Wales, Sydney 2052, Australia*

Jiaxin Lian − *School of Chemistry and Australian Centre for NanoMedicine, University of New South Wales, Sydney 2052, Australia*

Soshan Cheong − *Mark Wainwright Analytical Centre, University of New South Wales, Sydney 2052, Australia;* orcid.org/0000-0001-6133-0829

Peter B. O'Mara − *School of Chemistry and Australian Centre for NanoMedicine, University of New South Wales, Sydney 2052, Australia*

Kazeem O. Sulaiman − *Mark Wainwright Analytical Centre, University of New South Wales, Sydney 2052, Australia*

Cameron H. W. Kelly − *School of Chemistry and Australian Centre for NanoMedicine, University of New South Wales, Sydney 2052, Australia*

Robert W. J. Scott − *Department of Chemistry, University of Saskatchewan, Saskatoon, Saskatchewan S7N 5C9, Canada;* orcid.org/0000-0003-2155-7652

Complete contact information is available at: https://pubs.acs.org/10.1021/acscatal.0c05370

Author Contributions

The manuscript was written through contributions of all authors. All authors have given approval to the final version of the manuscript.

Notes

The authors declare no competing financial interest.

■ ACKNOWLEDGMENTS

This research was financially supported by the Australian Research Council of Centre of Excellence in Convergent Bio-

Nano Science and Technology (CE140100036), the ARC Australian Laureate Fellowship (FL150100060), and the Discovery Project (DP190102659 and DP200100143). R.W.J.S. acknowledges financial support from the National Sciences and Engineering Research Council of Canada. This work used the facilities supported by Microscopy Australia at the Electron Microscope Unit in the Mark Wainwright Analytical Centre at UNSW. XAS experiments were performed at Canadian Light Source, which is supported by the NSERC, the National Research Council Canada, the Canadian Institutes of Health Research, the Province of Saskatchewan, Western Economic Diversification Canada, and the University of Saskatchewan.

■ ABBREVIATIONS

MOR, methanol oxidation reaction

■ REFERENCES

(1) Antolini, E. Alloy vs. Intermetallic Compounds: Effect of the Ordering on the Electrocatalytic Activity for Oxygen Reduction and the Stability of Low Temperature Fuel Cell Catalysts. *Appl. Catal., B* **2017**, *217*, 201−213.

(2) Bauer, J. C.; Chen, X.; Liu, Q.; Phan, T.-H.; Schaak, R. E. Converting Nanocrystalline Metals into Alloys and Intermetallic Compounds for Applications in Catalysis. *J. Mater. Chem.* **2008**, *18*, 275−282.

(3) Wang, D.; Xin, H. L.; Hovden, R.; Wang, H.; Yu, Y.; Muller, D. A.; Disalvo, F. J.; Abruña, H. D. Structurally Ordered Intermetallic Platinum-Cobalt Core-Shell Nanoparticles with Enhanced Activity and Stability as Oxygen Reduction Electrocatalysts. *Nat. Mater.* **2013**, *12*, 81−87.

(4) Gamler, J. T. L.; Ashberry, H. M.; Skrabalak, S. E.; Koczkur, K. M. Random Alloyed versus Intermetallic Nanoparticles: A Comparison of Electrocatalytic Performance. *Adv. Mater.* **2018**, *30*, No. 1801563.

(5) Zou, L.; Fan, J.; Zhou, Y.; Wang, C.; Li, J.; Zou, Z.; Yang, H. Conversion of PtNi Alloy from Disordered to Ordered for Enhanced Activity and Durability in Methanol-Tolerant Oxygen Reduction Reactions. *Nano Res.* **2015**, *8*, 2777−2788.

(6) Li, Q.; Wu, L.; Wu, G.; Su, D.; Lv, H.; Zhang, S.; Zhu, W.; Casimir, A.; Zhu, H.; Mendoza-Garcia, A.; Sun, S. New Approach to Fully Ordered Fct-FePt Nanoparticles for Much Enhanced Electrocatalysis in Acid. *Nano Lett.* **2015**, *15*, 2468−2473.

(7) Wang, Z.; Yao, X.; Kang, Y.; Miao, L.; Xia, D.; Gan, L. Structurally Ordered Low-Pt Intermetallic Electrocatalysts toward Durably High Oxygen Reduction Reaction Activity. *Adv. Funct. Mater.* **2019**, *29*, No. 1902987.

(8) Zhou, M.; Li, C.; Fang, J. Noble-Metal Based Random Alloy and Intermetallic Nanocrystals: Syntheses and Applications. *Chem. Rev.* **2021**, *121*, 736−795.

(9) Chung, D. Y.; Chung, Y. H.; Jung, N.; Choi, K. H.; Sung, Y. E. Correlation between Platinum Nanoparticle Surface Rearrangement Induced by Heat Treatment and Activity for an Oxygen Reduction Reaction. *Phys. Chem. Chem. Phys.* **2013**, *15*, 13658−13663.

(10) Chung, Y. H.; Chung, D. Y.; Jung, N.; Park, H. Y.; Yoo, S. J.; Jang, J. H.; Sung, Y. E. Origin of the Enhanced Electrocatalysis for Thermally Controlled Nanostructure of Bimetallic Nanoparticles. *J. Phys. Chem. C* **2014**, *118*, 9939−9945.

(11) Poerwoprajitno, A. R.; Gloag, L.; Watt, J.; Cychy, S.; Cheong, S.; Kumar, P. V.; Benedetti, T. M.; Deng, C.; Wu, K.; Marjo, C. E.; Huber, D. L.; Muhler, M.; Gooding, J. J.; Schuhmann, W.; Wang, D. W.; Tilley, R. D. Faceted Branched Nickel Nanoparticles with Tunable Branch Lengthfor High-Activity Electrocatalytic Oxidation of Biomass. *Angew. Chem., Int. Ed.* **2020**, *59*, 15487−15491.

(12) Gloag, L.; Benedetti, T. M.; Cheong, S.; Li, Y.; Chan, X. H.; Lacroix, L. M.; Chang, S. L. Y.; Arenal, R.; Florea, I.; Barron, H.; Barnard, A. S.; Henning, A. M.; Zhao, C.; Schuhmann, W.; Gooding, J. J.; Tilley, R. D. Three-Dimensional Branched and Faceted Gold−Ruthenium Nanoparticles: Using Nanostructure to Improve Stability in Oxygen Evolution Electrocatalysis. *Angew. Chem., Int. Ed.* **2018**, *57*, 10241−10245.

(13) Alinezhad, A.; Gloag, L.; Benedetti, T. M.; Cheong, S.; Webster, R. F.; Roelsgaard, M.; Iversen, B. B.; Schuhmann, W.; Gooding, J. J.; Tilley, R. D. Direct Growth of Highly Strained Pt Islands on Branched Ni Nanoparticles for Improved Hydrogen Evolution Reaction Activity. *J. Am. Chem. Soc.* **2019**, *141*, 16202−16207.

(14) Wakisaka, M.; Suzuki, H.; Mitsui, S.; Uchida, H.; Watanabe, M. Increased Oxygen Coverage at Pt-Fe Alloy Cathode for the Enhanced Oxygen Reduction Reaction Studied by EC-XPS. *J. Phys. Chem. C* **2008**, *112*, 2750−2755.

(15) Peera, S. G.; Lee, T. G.; Sahu, A. K. Pt-Rare Earth Metal Alloy/Metal Oxide Catalysts for Oxygen Reduction and Alcohol Oxidation Reactions: An Overview. *Sustainable Energy Fuels* **2019**, *3*, 1866−1891.

(16) Stamenkovic, V. R.; Mun, B. S.; Mayrhofer, K. J. J.; Ross, P. N.; Markovic, N. M. Effect of Surface Composition on Electronic Structure, Stability, and Electrocatalytic Properties of Pt-Transition Metal Alloys: Pt-Skin versus Pt-Skeleton Surfaces. *J. Am. Chem. Soc.* **2006**, *128*, 8813−8819.

(17) Chen, H. S.; Benedetti, T. M.; Gonçales, V. R.; Bedford, N. M.; Scott, R. W. J.; Webster, R. F.; Cheong, S.; Gooding, J. J.; Tilley, R. D. Preserving the Exposed Facets of Pt_3Sn Intermetallic Nanocubes during an Order to Disorder Transition Allows the Elucidation of the Effect of the Degree of Alloy Ordering on Electrocatalysis. *J. Am. Chem. Soc.* **2020**, *142*, 3231−3239.

(18) House, C. I.; Kelsall, G. H. Potential—PH Diagrams for the Sn/H2O-Cl System. *Electrochim. Acta* **1984**, *29*, 1459−1464.

(19) Pietron, J. J.; Pomfret, M. B.; Chervin, C. N.; Long, J. W.; Rolison, D. R. Direct Methanol Oxidation at Low Overpotentials Using Pt Nanoparticles Electrodeposited at Ultrathin Conductive RuO 2 Nanoskins. *J. Mater. Chem.* **2012**, *22*, 5197−5204.

(20) Villullas, H. M.; Mattos-Costa, F. I.; Bulhões, L. O. S. Electrochemical Oxidation of Methanol on Pt Nanoparticles Dispersed on RuO2. *J. Phys. Chem. B* **2004**, *108*, 12898−12903.

(21) Lin, W. F.; Zei, M. S.; Eiswirth, M.; Ertl, G.; Iwasita, T.; Vielstich, W. Electrocatalytic Activity of Ru-Modified Pt(111) Electrodes toward CO Oxidation. *J. Phys. Chem. B* **1999**, *103*, 6968−6977.

(22) Lee, M. J.; Kang, J. S.; Kang, Y. S.; Chung, D. Y.; Shin, H.; Ahn, C. Y.; Park, S.; Kim, M. J.; Kim, S.; Lee, K. S.; Sung, Y. E. Understanding the Bifunctional Effect for Removal of CO Poisoning: Blend of a Platinum Nanocatalyst and Hydrous Ruthenium Oxide as a Model System. *ACS Catal.* **2016**, *6*, 2398−2407.

(23) Robinson, J. E.; Labrador, N. Y.; Chen, H.; Sartor, B. E.; Esposito, D. V. Silicon Oxide-Encapsulated Platinum Thin Films as Highly Active Electrocatalysts for Carbon Monoxide and Methanol Oxidation. *ACS Catal.* **2018**, *8*, 11423−11434.

(24) Tian, M.; Wu, G.; Chen, A. Unique Electrochemical Catalytic Behavior of Pt Nanoparticles Deposited on TiO_2 Nanotubes. *ACS Catal.* **2012**, *2*, 425−432.

(25) Unmüssig, T.; Melke, J.; Fischer, A. Synthesis of Pt@TiO_2 Nanocomposite Electrocatalysts for Enhanced Methanol Oxidation by Hydrophobic Nanoreactor Templating. *Phys. Chem. Chem. Phys.* **2019**, *21*, 13555−13568.

(26) Xu, C.; Pei, K. S. Novel Pt/CeO_2/C Catalysts for Electrooxidation of Alcohols in Alkaline Media. *Chem. Commun.* **2004**, *10*, 2238−2239.

(27) Xu, H.; Wang, A. L.; Tong, Y. X.; Li, G. R. Enhanced Catalytic Activity and Stability of Pt/CeO_2/PANI Hybrid Hollow Nanorod Arrays for Methanol Electro-Oxidation. *ACS Catal.* **2016**, *6*, 5198−5206.

(28) Xu, F.; Cheng, K.; Yu, Y.; Mu, S. One-Pot Synthesis of Pt/CeO2/C Catalyst for Enhancing the SO2 electrooxidation. *Electrochim. Acta* **2017**, *229*, 253−260.

https://dx.doi.org/10.1021/acscatal.0c05370
ACS Catal. 2021, 11, 2235−2243

(29) Yang, X.; Wang, X.; Zhang, G.; Zheng, J.; Wang, T.; Liu, X.; Shu, C.; Jiang, L.; Wang, C. Enhanced Electrocatalytic Performance for Methanol Oxidation of Pt Nanoparticles on Mn3O4-Modified Multi-Walled Carbon Nanotubes. *Int. J. Hydrogen Energy* **2012**, *37*, 11167−11175.
(30) Jiménez-Morales, I.; Cavaliere, S.; Jones, D.; Rozière, J. Strong Metal-Support Interaction Improves Activity and Stability of Pt Electrocatalysts on Doped Metal Oxides. *Phys. Chem. Chem. Phys.* **2018**, *20*, 8765−8772.
(31) Liu, D.; Zhang, L.; Du, Y.; Cui, S.; Jie, W.; Jin, Z. Development of an Atomic Mobility Database for Disordered and Ordered Fcc Phases in Multicomponent Al Alloys: Focusing on Binary Systems. *Int. J. Mater. Res.* **2013**, *104*, 135−148.
(32) Liu, Y.; Wei, M.; Raciti, D.; Wang, Y.; Hu, P.; Park, J. H.; Barclay, M.; Wang, C. Electro-Oxidation of Ethanol Using Pt3Sn Alloy Nanoparticles. *ACS Catal.* **2018**, *8*, 10931−10937.
(33) Wang, Z.; Yao, X.; Kang, Y.; Miao, L.; Xia, D.; Gan, L. Structurally Ordered Low-Pt Intermetallic Electrocatalysts toward Durably High Oxygen Reduction Reaction Activity. *Adv. Funct. Mater.* **2019**, *29*, No. 1902987.
(34) Cui, Z.; Chen, H.; Zhou, W.; Zhao, M.; Disalvo, F. J. Structurally Ordered Pt_3Cr as Oxygen Reduction Electrocatalyst: Ordering Control and Origin of Enhanced Stability. *Chem. Mater.* **2015**, *27*, 7538−7545.
(35) Koh, S.; Toney, M. F.; Strasser, P. Activity-Stability Relationships of Ordered and Disordered Alloy Phases of Pt_3Co Electrocatalysts for the Oxygen Reduction Reaction (ORR). *Electrochim. Acta* **2007**, *52*, 2765−2774.
(36) Chung, D. Y.; Lee, K. J.; Sung, Y. E. Methanol Electro-Oxidation on the Pt Surface: Revisiting the Cyclic Voltammetry Interpretation. *J. Phys. Chem. C* **2016**, *120*, 9028−9035.
(37) Zeng, R.; Yang, Y.; Shen, T.; Wang, H.; Xiong, Y.; Zhu, J.; Wang, D.; Abruña, H. D. Methanol Oxidation Using Ternary Ordered Intermetallic Electrocatalysts: A DEMS Study. *ACS Catal.* **2020**, *10*, 770−776.
(38) Qi, Z.; Xiao, C.; Liu, C.; Goh, T. W.; Zhou, L.; Maligal-Ganesh, R.; Pei, Y.; Li, X.; Curtiss, L. A.; Huang, W. Sub-4 Nm PtZn Intermetallic Nanoparticles for Enhanced Mass and Specific Activities in Catalytic Electrooxidation Reaction. *J. Am. Chem. Soc.* **2017**, *139*, 4762−4768.
(39) Feng, Q.; Zhao, S.; He, D.; Tian, S.; Gu, L.; Wen, X.; Chen, C.; Peng, Q.; Wang, D.; Li, Y. Strain Engineering to Enhance the Electrooxidation Performance of Atomic-Layer Pt on Intermetallic Pt_3Ga. *J. Am. Chem. Soc.* **2018**, *140*, 2773−2776.
(40) Rizo, R.; Pastor, E.; Koper, M. T. M. CO Electrooxidation on Sn-Modified Pt Single Crystals in Acid Media. *J. Electroanal. Chem.* **2017**, *800*, 32−38.
(41) Farias, M. J. S.; Cheuquepán, W.; Tanaka, A. A.; Feliu, J. M. Nonuniform Synergistic Effect of Sn and Ru in Site-Specific Catalytic Activity of Pt at Bimetallic Surfaces toward CO Electro-Oxidation. *ACS Catal.* **2017**, *7*, 3434−3445.
(42) Kowal, A.; Li, M.; Shao, M.; Sasaki, K.; Vukmirovic, M. B.; Zhang, J.; Marinkovic, N. S.; Liu, P.; Frenkel, A. I.; Adzic, R. R. Ternary Pt/Rh/SnO2 Electrocatalysts for Oxidizing Ethanol to CO2. *Nat. Mater.* **2009**, *8*, 325−330.
(43) Zhang, J.; Vukmirovic, M. B.; Sasaki, K.; Nilekar, A. U.; Mavrikakis, M.; Adzic, R. R. Mixed-Metal Pt Monolayer Electrocatalysts for Enhanced Oxygen Reduction Kinetics. *J. Am. Chem. Soc.* **2005**, *127*, 12480−12481.
(44) Masuda, T.; Fukumitsu, H.; Fugane, K.; Togasaki, H.; Matsumura, D.; Tamura, K.; Nishihata, Y.; Yoshikawa, H.; Kobayashi, K.; Mori, T.; Uosaki, K. Role of Cerium Oxide in the Enhancement of Activity for the Oxygen Reduction Reaction at Pt-CeO_x Nanocomposite Electrocatalyst - An in Situ Electrochemical X-Ray Absorption Fine Structure Study. *J. Phys. Chem. C* **2012**, *116*, 10098−10102.
(45) Park, E. D.; Lee, D.; Lee, H. C. Recent Progress in Selective CO Removal in a H2-Rich Stream. *Catal. Today* **2009**, *139*, 280−290.
(46) Yang, X.; Kattel, S.; Senanayake, S. D.; Boscoboinik, J. A.; Nie, X.; Graciani, J.; Rodriguez, J. A.; Liu, P.; Stacchiola, D. J.; Chen, J. G. Low Pressure CO_2 Hydrogenation to Methanol over Gold Nanoparticles Activated on a CeOx/TiO_2 Interface. *J. Am. Chem. Soc.* **2015**, *137*, 10104−10107.
(47) Chmielniak, T.; Sciazko, M. Co-Gasification of Biomass and Coal for Methanol Synthesis. *Appl. Energy* **2003**, *74*, 393−403.
(48) Grozovski, V.; Climent, V.; Herrero, E.; Feliu, J. M. The Role of the Surface Structure in the Oxidation Mechanism of Methanol. *J. Electroanal. Chem.* **2011**, *662*, 43−51.
(49) Wang, X.; Altmann, L.; Stöver, J.; Zielasek, V.; Bäumer, M.; Al-Shamery, K.; Borchert, H.; Parisi, J.; Kolny-Olesiak, J. Pt/Sn Intermetallic, Core/Shell and Alloy Nanoparticles: Colloidal Synthesis and Structural Control. *Chem. Mater.* **2013**, *25*, 1400−1407.
(50) Li, D.; Wang, C.; Tripkovic, D.; Sun, S.; Markovic, N. M.; Stamenkovic, V. R. Surfactant Removal for Colloidal Nanoparticles from Solution Synthesis: The Effect on Catalytic Performance. *ACS Catal.* **2012**, *2*, 1358−1362.
(51) Zhang, J.; Fang, J. A General Strategy for Preparation of Pt 3d-Transition Metal (Co, Fe, Ni) Nanocubes. *J. Am. Chem. Soc.* **2009**, *131*, 18543−18547.
(52) Chiu, H. C.; Yeh, C. S. Hydrothermal Synthesis of SnO_2 Nanoparticles and Their Gas-Sensing of Alcohol. *J. Phys. Chem. C* **2007**, *111*, 7256−7259.
(53) Ravel, B.; Newville, M. {\it ATHENA}, {\it ARTEMIS}, {\it HEPHAESTUS}: Data Analysis for X-Ray Absorption Spectroscopy Using {\it IFEFFIT}. *J. Synchrotron Radiat.* **2005**, *12*, 537−541.
(54) Rudi, S.; Cui, C.; Gan, L.; Strasser, P. Comparative Study of the Electrocatalytically Active Surface Areas (ECSAs) of Pt Alloy Nanoparticles Evaluated by Hupd and CO-Stripping Voltammetry. *Electrocatalysis* **2014**, *5*, 408−418.

https://dx.doi.org/10.1021/acscatal.0c05370
ACS Catal. 2021, 11, 2235−2243